Journal of Volcanology and Geothermal Research 454 (2024) 108164

Contents lists available at ScienceDirect

Journal of Volcanology and Geothermal Research

journal homepage: www.journals.elsevier.com/journal-of-volcanology-and-geothermal-research

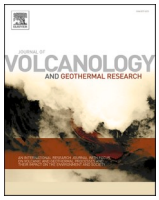

Constraining proximal grainsize distribution of tephra from paroxysmal eruptions at Etna volcano

Francesco Amadio [a,*], Laura Pioli [a], Simona Scollo [b]

[a] Dipartimento di Scienze Chimiche e Geologiche, Università di Cagliari, Cittadella Universitaria, Monserrato 09042, Italy
[b] Istituto Nazionale di Geofisica e Vulcanologia, Osservatorio Etneo, Piazza Roma 2, 95125 Catania, Italy

ARTICLE INFO

Keywords:
Tephra deposition
Stratigraphic correlation
Tephra hazard

ABSTRACT

This study examines proximal deposits associated with 17 lava fountains occurring at the South-East Crater between 16/02 and 1/04, 2021. This eruptive crisis gave rise to some of the most intense eruptions at Etna in the last decade. We studied products deposited from 1 to 3.2 km to the south of the vent. Tephra was preserved within and at the top of the snowpack and layers were correlated based on eruption chronology, remote sensing data on the plume dispersal, and precipitation chronology. The grainsize distribution of these proximal and ultra-proximal deposits is multimodal, with Mdϕ ranging from −2.79 and − 1.84, and σϕ 1.34 and 1.80. Refined data (50% of the main population range between Mdϕ −2.63 and − 1.63ϕ, and σϕ 1.01 and 1.41) were used in a comparative study with existing datasets for selected eruptions to assess the representativity of our data and define a Mdϕ/distance correlation along the dispersal axis. Finally, the contribution of proximal data on the total grainsize distribution suggest that they significantly affect the median grainsize values. A complete sampling could decrease it by up to 2 phi units when compared to distribution based only on medial to distal sampling. Results from this study reinforce the importance of collecting samples in proximal areas.

1. Introduction

Mafic magmas, despite their relatively low viscosity (Sparks et al., 1994; Parfitt, 1998), are capable of producing considerably explosive eruptions. Typical explosive eruptive styles of mafic volcanism span from discrete Strombolian explosions to sustained lava fountains and paroxysm (Taddeucci et al., 2015, The Encyclopedia of Volcanoes, chapter 27, Hawaiian and Strombolian Eruptions, pp. 485–503; Edwards et al., 2018). All these mild explosive activities are frequently marked by formation of weak to strong plumes (Bonadonna and Phillips, 2003; Bonadonna et al., 2015b). Assessment of the hazard associated with explosive mafic activity requires not only an accurate description of the variability of eruptive manifestations but the use of properly scaled eruption models. Most volcanic ash dispersion and sedimentation predictive models are based on eruptions of a larger scale intensity (i.e. Sub-Plinian to Plinian - FALL3D Costa et al., 2006; VOL-CALPUFF Barsotti et al., 2008; Folch, 2012; HYSPLIT Stein et al., 2015). For this reason, these models are not always capable of accurately describing smaller (VEI = 2–3) eruptions in terms of both mass load and the distribution of particles into the atmosphere (Scollo et al., 2008a). Moreover, a notable uncertainty of input parameters (Eruption Source Parameters ESP, Mastin et al., 2009) also significantly affects the model results (Scollo et al., 2008b; Bonadonna et al., 2015a). Some of the critical input parameters are linked to the grainsize distribution of the tephra emitted during explosive eruptions controlling tephra dispersion and sedimentation (Scollo et al., 2008a; Bonadonna and Costa, 2013).

The particle grain size distribution (GSD) is not only of crucial importance but is also the most difficult parameter to constrain (Scollo et al., 2019; Pioli et al., 2019). Real-time measurements can be the ideal technique to assess the GSD (Pioli and Harris, 2019) but, unfortunately, no instrument is able to provide a satisfactory estimate at the vent yet. For this reason, measurements are based on field-base strategies (Scollo et al., 2019). Instead, the Total Grain-Size Distribution (TGSDs) is considered as equal to the weighted average of the individual particle size distributions of the various tephra samples taken at different distances from both the vent and the dispersion axis of the eruptive plume. The accuracy of data collection is fundamental. In most cases, the samples are collected only from medial or distal areas because of inaccessibility or poor preservation of deposits in proximal locations (Andronico et al., 2014a). In these cases, TGSD is affected by the lack of proximal or ultra-proximal data, leading to a large uncertainty in its estimation.

* Corresponding author.
E-mail address: francesco.amadio@unica.it (F. Amadio).

https://doi.org/10.1016/j.jvolgeores.2024.108164
Received 18 March 2024; Received in revised form 18 June 2024; Accepted 7 August 2024
Available online 9 August 2024

In this paper, we investigate proximal deposition of tephra from lava fountains to better constrain its contribution to TGSD. We selected Mt. Etna as a type case because of the high frequency of its eruptions, extensive monitoring, and large available dataset. Explosive activity at Etna spans from Strombolian events to lava fountains and violent Strombolian events. Sub-Plinian and Plinian events are much less frequent (i.e. 1998 eruption, Andronico et al., 1999; 122 BCE and 3930 B.P. eruptions, Coltelli et al., 1998, 2000, 2005).

We present a study of very proximal deposits from a series of paroxysmal eruptions between February and April 2021 at the South-East Crater (SEC). These lava fountains were also associated with lava flows from 2 to 4 km long, which poured into the "Valle del Bove", "Valle del Leone" and in the south-western sector through the "Bocca della Sella" fracture. Throughout this period, the other craters showed intense degassing and intracrater explosive activity with sporadic emissions of ash (INGV-OE monitoring reports from 16/02/2021 to 06/04/2021 in www.ct.ingv.it).

2. Volcano Etna activity

Among the most active volcanoes in the world, Etna is known for its persistent and highly variable mafic eruptive activity. It was traditionally considered a predominantly effusive volcano characterized mainly by the emission of lava flows (Branca et al., 2013, 2017). In the last three centuries, there has been an increase in the frequency of explosive eruptive episodes from summit craters, ranging in scale from Strombolian to more energetic episodes such as lava fountains (i.e. Etna eruptions of 2000–2001, 2002–2003 2011–2012, Alparone et al., 2003; Branca and Del Carlo, 2005; Scollo et al., 2007; Andronico et al., 2009; Behncke et al., 2014) and subplinian eruptions (for example, the 1990 and 1998 eruptions; Andronico et al., 1999; Scollo et al., 2013).

Etna's eruptive behavior is often very complex and can vary from months or years when eruptive activity is concentrated at a single summit crater (i.e. August–December 2006, Andronico et al., 2014b) or may involve multiple craters (i.e. 2011–2013 eruptions; Viccaro et al., 2015; 2016 eruption; Edwards et al., 2018; Edwards and Pioli, 2019). The Plinian eruption of 122 B.C. (Coltelli et al., 1998) highlights the highly variable behavior of this volcano.

Etna is currently believed to be in a relatively stationary phase, with major eruptive episodes occurring fairly regularly with a frequency of several months to a year and with a similar pattern (Calvari et al., 2021; Bonaccorso et al., 2021). Over the past 50 years, Etna has continued to alternate between effusive activity with sustained lava flows and transient (hours-days) or long-lasting (weeks-months) explosive activity

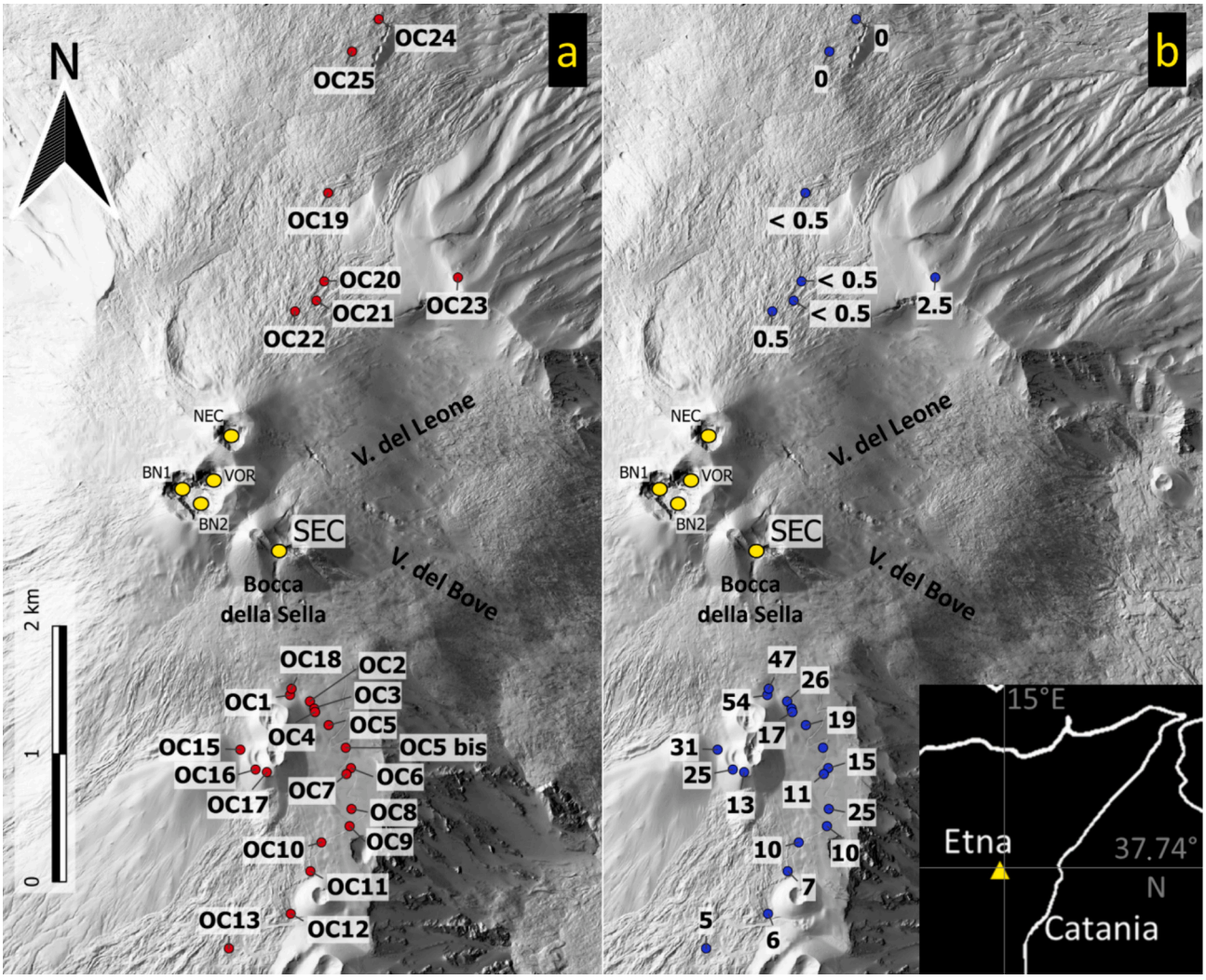

Fig. 1. DTM Map of Etna's summit area showing: the summit craters (yellow circles: BN1–2 = BoccaNuova1–2; NEC=North-East Crater; VOR = Voragine; SEC=South-East Crater); the sampling sites reported in the text (red circles in a) and the total deposit thickness (cm) measured in each site (blue circles in b). The inset shows a schematic map of North-East Sicily and the location of Mt. Etna (yellow triangle). (For interpretation of the references to colour in this figure legend, the reader is referred to the web version of this article.)

(Andronico et al., 2021). Paroxysmal episodes lasting a few hours each in which one (or more) of the summit craters are involved, are usually associated with the formation of eruptive columns up to 7–12 km above vent (a.v.) and active lava flows (Andronico et al., 2014a).

In recent decades, explosive activity has typically occurred at the summit vents (Fig. 1). In paroxysmal eruptions, Strombolian activity evolves into lava fountains that last from tens of minutes to hours and are often accompanied by lava flows (Alparone et al., 2003; Polacci et al., 2006). This activity can be a threat to local communities and cause damage to property, agriculture, infrastructures and air traffic (Blong, 1984; Casadevall, 1994; Guffanti et al., 2009). Based on the INGV-OE (Istituto Nazionale di Geofisica e Vulcanologia, Osservatorio Etneo, Catania) monitoring network present on Etna, most of these eruptions have been extensively studied, leading to a better understanding of the eruptive dynamics of explosive basaltic eruptions.

2.1. Etna 2020–21 activity

The February–April 2021 eruptive crisis was the culmination of a phase that began about a year earlier. Based on monitoring (from 1/01/2020 to 12/31/2021) of SO_2 fluxes, Aiuppa et al. (2023) recognized a first precursory phase characterized by a lack of visible eruptive activity at the South-East Crater (SEC) and mild Strombolian activity at the SEC and Voragine (VOR) craters (Fig. 1). Then, from May to December 2020, a second precursory phase occurred, which identifies the resumption of the SEC volcanic activity and its gradual intensification (although remaining characterized by a mild Strombolian activity and scattered ash emission events), with an increase in outgassing at SEC in the last two months.

The eruption of 13/12/20 marked the beginning of a new sequence characterized by >60 eruptive episodes (Calvari and Nunnari, 2022). Marked explosive activity occurred after the lava fountain of 16/02/21, forming tephra plumes, some of them higher than 7 km above the vent. Between February and April 17, paroxysmal episodes occurred. Those events occurred only a few days apart and ended abruptly with the eruption of 31/03–1/04/2021, followed by about 2 months of relative quiescence (no paroxysms). All eruptive events in this period took place at the SEC, but throughout this time the other summit craters still showed mild intracrater explosive activity (Andronico et al., 2021; Bonaccorso and Aloisi, 2021; Marchese et al., 2021; Corsaro and Miraglia, 2022). During some of these paroxysms, small scale pyroclastic flows were also generated from the partial collapse of the SEC walls.

The chronology of eruptive events during the period is derived from the INGV-OE monitoring reports (https://www.ct.ingv.it/index.php/monitoraggio-e-sorveglianza/prodotti-del-monitoraggio/bollettini-settimanali-multidisciplinari).

3. Materials and methods

For this work, a total of 31 samples were taken from 18 sites located on the southern and northern flanks of the SEC (samples from proximal areas from 1 to 3.2 km from the vent).

3.1. Stratigraphic correlation and sampling

A field campaign was undertaken from 4/05 to 11/052021, 33 days after the last fountain on 1/04. Snow was still covering the summit area and preserved in patches down to 2500 m asl. Trenches were dug in the snow to expose stratigraphy down to the basal snow layer and the soil. We analyzed stratigraphic sequences from 18 sites at distances ranging from 1 to 3.2 km from the vent (Fig. 1) on the northern and southern part of the SEC and collected 33 samples. These sites are aligned approximately North-South. Their total thickness (comprising the snow between ash layers) varies from 1.5 m in the more distal outcrops to 3 m in the outcrops closest to the crater. Etna's northern flank was also the subject of the sampling campaign. Seven sites were investigated in this area at distances ranging from 2 to 4 km from the SEC, aligned in an approximately North/North-East direction from the SEC, but only 3 samples were taken because the tephra deposits were very thin and not preserved in snow.

A stratigraphic correlation between trenches was made comparing eruptive chronology, weather data (referring to the Etna station and available online at https://www.3bmeteo.com/meteo/etna/storico/202102), and plume dispersal as recorded by satellite sensors from SEVIRI (Spinning Enhanced Visible and InfraRed Imager, available on https://view.eumetsat.int - access on 14/02/2024) and MultiSpectral Instrument sensor (MSI on Sentinel-2, available on https://www.mirovaweb.it, Massimetti et al., 2020) and implemented in recursive steps to ensure a coherent reconstruction. The data collected by the SEVIRI instrument on board Meteosat Second Generation (MSG) geostationary satellite, available on the Eumetview platform, were used to visualize the direction of dispersion of volcanic plumes (RGB product of volcanic ash), thus helping understand whether sedimentation occurred in our study area (Guerrieri et al., 2023). The MSI sensor aboard the Sentinel2 series of satellites is a wide-swath, high-resolution, multi-spectral imaging sensor which is useful for land monitoring studies. The mirova platform provides false colour RGB images (R:2.2um, G:1.6um, B:0.8um) which helped us recognize the volcanic products that were deposited above the snow layer, revealing the area of sedimentation (Marchese et al., 2019).

3.2. Physical characterization of tephra

Samples were dried at 80 °C for at least 24 h and then hand sieved at half ϕ intervals from −5.5 to 1 phi. The total amount of the samples (ranging in weight between 0.1 and 1.5 kg) was used for this analysis, without quartering steps and proceeding by small quantities of material so as not to obstruct the meshes of the sieves or break the pyroclasts. Finer fractions were then analyzed using a laser diffraction particle size analyzer (Malvern® Mastersizer 3000). Grain-Size parameters such as the median diameter (Mdϕ), sorting (σϕ; Inman, 1952), F1 F2 (F1 Wt% of particles finer than 1 mm, F2 Wt% of particles finer than 1/16 mm – 63 μm; Walker, 1983) were calculated from raw data. Further statistical analyses were performed to identify grainsize subpopulations. Deconvolution of the curves was done assuming a lognormal distribution of wt % vs particle diameter (i.e. gaussian in ϕ; Wohletz et al., 1989) using the Curvefitter application of the software Matlab © (https://it.mathworks.com/help/curvefit/curvefitter-app.html). In this work, we consistently used this distribution because it best reproduces the shape of our multimodal samples and can distinguish the various grain-size populations that may result from distinct sedimentation processes. Median and standard deviation of the subpopulations were then considered for sample characterization.

The site OC5 was chosen as the type sequence to perform density, shape, and componentry analyses.

Component analyses were performed on the coarse material of all layers found in site OC5 (see Table 2) from −5.5ϕ (45.25 mm where present) down to 0 ϕ (1 mm). Shape and density analyses were performed on the OC5-1b sample (Table 2) taken from the layer E8, starting from the coarsest material (−5ϕ, 32 mm) down to sizes -3ϕ (8 mm, shape analyses) and − 3.5ϕ (11.2 mm, density analyses). A total of 84 clasts were analyzed for shape analysis and 58 clasts were analyzed for density analysis.

The samples were first dried at 80 °C for 24 h and weighed, then sealed by immersion in a solution of acetone and cellulose acetate and dried in a fume hood for 24 h, following Polacci et al. (2003). They were then weighed again in air to measure the weight of the coating. Volume was measured by hydrostatic weight at 26.5 °C and compared with weight to calculate density.

3.3. Dataset

For comparative purposes, we selected published data from 15 documented eruptions at Etna volcano between 2001 and 2022 (Table and references presented as supplementary materials, Table S1), associated with columns whose heights range from 1.2 to 11 km above the active vent. Grainsize and eruption information were collected from the published articles where this information was available. In addition, we chose only events in which the eruptive column height was known, and possibly directly measured (i.e. satellite-based measurements or high-resolution cameras) to better compare with our case study. In most cases (i.e. 12–13/01/2011 eruption, Andronico et al., 2014a), we considered only data collected along the plume dispersal axis.

4. Results

4.1. The February – April 2021 eruption sequence

Results of the comparative analyses of reports and remote sensing data of the February–April 2021 activity are reported in Table 1. The paroxysms formed lava fountains up to 1.5 km high, generating eruptive plumes up to about 8 km a.v. and lava flows which flowed mainly to the E into the "Valle del Bove".

4.2. Stratigraphy of tephra deposits

The sites investigated on the northern flank of Etna showed layers that vary in thickness between 0 and 0.5 cm and are composed of fine ash. Only one site, located further east than the others at 2.5 km from SEC, has a thickness of 2.5 cm (Figs. 2,3, Table 1).

By contrast, each trench analyzed in the southern flank exposed 1 to 6 tephra beds separated by snow/ice layers. Satellite data and INGV reports suggest that 5 out of 17 eruptions occurring from January to March deposited material on the Southern flank (Fig. 4, Table 1); we therefore identified them as the main events preserved in the sequences. Only 3 eruptions result in an almost northward dispersion direction and are related to 1 up to 3 very thin layers found in the Northern sector and whose thickness varies from 0 to 0.5 cm (linked to the deposition from the 4/03, 7/03 and 10/03 eruptions, Table 1).

1 to 2 mm-thick, red fine ash beds were identified in several sites (Fig. 2). The lowermost layer was isolated in the snowpack and below any tephra layer and was correlated with the density current associated with the eruption of 13–14/12/2020, which dispersed tephra in a South-East direction, and was then disregarded from further analyses, while the upper layer, often preserved at the base of a tephra bed was considered as the first deposit of the January–April eruptive sequence (E1, Fig. 5 and Table 1). In sites located from 1.9 to 2.5 km from the vent,

Table 1
Sequence of the paroxysmal events occurring during Etna's February–April 2021 eruptive crisis. Reports on the eruption durations and column heights are available on the INGV-OE website (www.ct.ingv.it) as reports and bulletins and in the VONA reports, respectively (Corradini et al., 2018; Scollo et al., 2019).

Name	Eruption date	Fountain duration	H column (Km a. v.)	Density Current	Plume axis	Stratigraphy
E1	16/02/2021	35 min; 50 min (INGV)	7	Ran along the westernmost edge of Valle del Bove	S-SSE	A thick layer of snow had deposited in the previous week, and the deposit is clearly distinguishable from satellite images. A thin layer of red fine ash is interpreted as deposited from the syneruptive pyroclastic flow associated with cone collapse.
E2	17–18/02/2021	45 min; 60 min (INGV)	7	–	SE	Dispersion axis is slightly more toward east with respect to the investigated area. Possibly a thin layer of ash from the edges of the plume had deposited in the area.
E3	19/02/2021	65 min; 1:14 h (INGV)	7	–	SE	Dispersion axis is slightly more toward east with respect to the investigated area. Possibly a thin layer of ash had deposited from the edges of the plume.
E4	20–21/02/2021	180 min; 3:20 h (INGV)	7	–	W-WSW	The investigated area is outside the plume region.
E5	22–23/02/2021	50 min	>7	–	NW	The investigated area is outside the plume region.
E6	24/02/2021	140 min; 2:20 h (INGV)	8	Ran toward East-Through Valle del Bove	NNW	The investigated area is outside the plume region. There is no evidence of deposition from the density current in the deposits studied.
E7	28/02/2021	54 min	8	2 flows (to SO; E)	*E*-ESE	The investigated area is outside the plume region. There is no evidence of deposition from the density current in our deposits.
E8	2/03/2021	12 min	>6	–	S-SSE	From 21 to 24/02/2021 at least 10 cm of snow had deposited (and partially melted). Only one outcrop recorded this snow layer and allowed distinguishing tephra associated with this eruption.
E9	4/03/2021	130 min	8	–	NE	The investigated area is outside the plume region.
E10	7/03/2021	1 h	7	–	E-ENE	The investigated area is outside the plume region.
E11	10/03/2021	163 min	6–7	–	E-ENE	The investigated area is outside the plume region.
E12	12/03/2021	175 min	6–7	–	E-ESE	The investigated area is outside the plume region.
E13	14–15/03/2021	170 min	n.a.	–	SE	In the previous week at least 50 cm of snow had deposited (and partially melted). Dispersion axis is slightly more toward east with respect to the investigated area. This eruption was recorded in the stratigraphy as a thin layer of fine ash between 2 layers of snow.
E14	17/03/2021	170 min	n.a.	–	S-SSE	In the previous 2 days at least 60 cm of snow had deposited (and partially melted). This eruption has been recorded by our deposits as a layer of ash between 2 layers of snow.
E15	19/03/2021	120 min	n.a.	–	E-ENE	The investigated area is outside the plume region.
E16	23–24/03/2021	480 min	3–4	Ran along the westernmost edge of Valle del Bove	S	In the previous week a thick layer of snow had deposited (and partially melted). The deposit is clearly distinguishable from satellite images. A thin layer of red fine ash records the deposition from pyroclastic flow.
E17	31/03/2021 1/04/2021	540 min	6	–	S-SSW	No stratigraphic evidence can be used to separate this eruption from the previous one.

During this entire period temperature recorded at Etna weather station remained constantly below 0 °C.

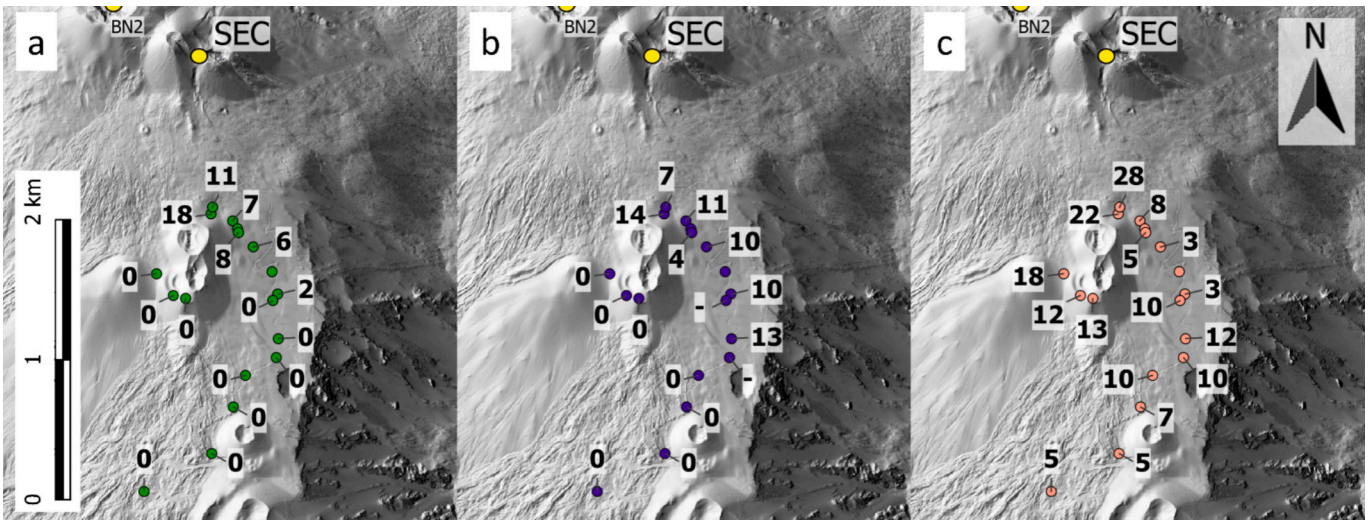

Fig. 2. DTM map showing the location of the studied trenches and the thickness of layers E1 (a) E8 (b) and E16–17 (c). The yellow circle indicates the location of the SEC which generated the eruptions that built up the analyzed deposits. (For interpretation of the references to colour in this figure legend, the reader is referred to the web version of this article.)

two fine red ash beds not always directly overlain by tephra were preserved; because of their relative position within the stratigraphy, we correlate both to the studied eruptive sequence.

The most complete stratigraphic log was found at site OC 18, preserving four tephra layers within the snowpack. Two main scoria levels with multiple grading were present in most trenches. Two minor coarse ash beds are buried in between the two scoria levels. Further down the volcano slope, the sequences are formed by either 2 or 3 lapilli scoria layers. From 1.9 to 2.5 km from the vent (sites OC7 to OC12 except for OC8) the sequence is reduced to a single tephra bed at the top of the snowpack.

4.3. Componentry

The tephra samples analyzed show a predominance of juvenile material with respect to lithic material. The following components can be recognized: (I) black tachylite clasts with fresh, shiny, unaltered glassy surface. They have irregular shape and moderate vesicularity. (II) brown sideromelane clasts with fresh, unaltered glassy surface, irregular shape but greater vesicularity and smaller vesicles than tachylite (sideromelane and tachylite after Taddeucci et al., 2002). (III) gray scoria clasts, holocrystalline with an opaque surface tending to gray and a more irregular shape than the previous classes; (IV) lithic clasts showing surface alteration, with colour that can vary from gray to red, probably resulting from recycling of material of the SEC cone. (V) free, euhedral crystals (plagioclase, pyroxene, olivine) found in the finest grain size classes analyzed.

Tachylite scoria appear to be the most abundant in all the samples analyzed (90–98 wt%) followed by sideromelane, whose relative abundance increases slightly in the finer grain-sizes (1–6 wt%). Lithic fragments (gray and altered scoria) and crystals were predominantly found in the fine grain sizes, but with percentages always below 1 wt%.

4.4. Clast morphology and density

The classification of lapilli shapes was based on the scheme proposed by Sneed and Folk (1958). Most of the clasts analyzed fall into the Compact-Bladed class (CB 26.2%). The Compact-Platy (CP) and Compact-Elongate (CE) classes both comprise 16.7% of the analyzed material, while the Compact (C) class 15.5%. The other classes have percentage values of <10% (Fig. 6).

No clear trend emerges from density measurements. In the analyzed grain sizes, density increases as analyzed clast volume decreases, with an average value of 1.28 g/cm^3. Vesicularity was calculated based on Dense Rock Equivalent (DRE, clast powder density) values of 2890 kg/m^3 (Edwards et al., 2018; Edwards and Pioli, 2019) varies from "low" to "moderate" and only in some cases is it "high" (following Houghton and Wilson, 1989), confirming the heterogeneity found in density measurements.

4.5. Grainsize distribution of tephra

Grainsize distributions of tephra sampled at all sites are multimodal. The calculated normal distribution main mode is the central one (ϕ sizes ranging from −3.3 and − 1.1) followed by a secondary mode at around 1 ϕ and, for some layers, a third mode at coarse grainsizes (larger than -4ϕ). Granulometric statistical parameters Mdϕ and σϕ of the analyzed tephra layers are listed in Table 2 (and Table S2 in supplementary material provides other useful information) and Mdϕ range from −4.09 to −0.54. Sorting varies from 2.38 to 0.8. The fine ash fraction (F2) is generally <1% wt. of the sample.

Empirical distributions were treated as a sum of secondary grainsize subpopulations based on the theory of Sheridan and Wohletz (i.e. assuming lognormal distribution for each deposition 'unit', Sheridan et al., 1987; Wohletz et al., 1989). The coarse mode (i.e. above −5 phi) was not considered for calculations as poorly described in the empirical distribution. Subpopulations are then associated to the intermediate and fine-grained modes (Fig. 7) cluster into more definite areas: the main subpopulation shows $Md\phi$ (−2.63 and − 1.63) and $\sigma\phi$ (1.01 and 1.41) and sorting increases with Mdϕ. The fine subpopulation data distribute in a narrow $Md\phi$ range (from 0.74 to 1.1) with $\sigma\phi$ varying from 0.72 to 1.26 (Fig. 7).

Weighted average of tephra was calculated for the main layers (E1, E8 and E16–17, Fig. 8). Averaged GSDs are multimodal with similar main modes (−2.96 ϕ to −2.26 ϕ) and a secondary mode from 0.9 ϕ to 1.4 ϕ. A third coarse mode is visible only for the layers E1 and E8 and was not considered for statistical analysis because these are not clasts sedimented from the plume, but rather followed ballistic trajectories. The average GSD could be fitted either by a Weibull distribution (which does not reproduce the coarse mode but fits the general shape reasonably well) or two lognormal distributions (still not reproducing the coarse mode).

4.5.1. Comparative study

Because of its stability in all the analyzed samples the fine population is associated to aeolian remobilization (Folch et al., 2014; Liu et al., 2014; Panebianco et al., 2017; Del Bello et al., 2018; Dominguez et al., 2020; Jarvis et al., 2020) or it could be due to off-axis sedimentation of plumes formed by the lava fountains which dispersed outside the investigated area and not primarily recorded in the sequences (Bursik et al., 1992; Sparks et al., 1992; Bonadonna et al., 1998; Bonadonna and Phillips, 2003; Bonadonna et al., 2005). We will then analyze only the coarse population as we consider it as linked to the sedimentation of plumes from the events listed in Table 1 and shown Fig. 4.

For the comparative study, we compare grainsize of the coarse subpopulation with those of past Etna eruptions (table S1 in supplementary material). These eruptions are sorted based on column height and, for fitting analyses, divided into two main groups (column heights $<$ and $>$ 5 km above the vent). Fig. 9 shows that the literature dataset fits a power law distribution well. When including our proximal data, they satisfactorily follow the trend outlined by the highest intensity eruptions (H $>$ 5 km): including our data in the literature dataset does not change the fitting parameters significantly but slightly improves R^2 (Table 3). Data also fit with the trend defined by the smallest (H $<$ 5 km) eruption dataset, but with a larger gap from the most proximal data available (Fig. 9); in this case including our data R^2 parameter improves but also significantly changes the fitting parameters.

To estimate the contribution of proximal sedimentation to the grainsize distribution of the erupted tephra we base our calculations on the study of Andronico et al. (2008), which proposes a proximal sedimentation of 50–60% of the total tephra mass. As a type case, we add the computed grainsize distributions for layers E1, E8 and E16–17, to the 4–5/09/2007 eruption TGSD as measured by Andronico et al. (2008) based on medial to distal sampling. This eruption is a type case for Etna studies as most of the plumes disperse to the East and cannot be sampled in proximal locations because of the inaccessibility of the Valle del Bove. We added 40 to 60% of mass of particles with a distribution corresponding to our weighted distributions of proximal tephra layers. This results in a dramatic change of the total grainsize distribution, with Mdϕ decreasing by 2 ϕ units (Fig. 10).

5. Discussion

5.1. Stratigraphy of proximal tephra fall deposits of the February–April 2021 sequence

Based on eruption chronology and meteorological conditions at Etna summit, we deduce that the lower scoria bank formed during 4 events in the period between 16/02 (E1) to the 2/03 (E8). However, only 2 of these 4 eruption blankets cover all the sites under examination, while the others dispersed to the East, leaving the most distal outcrops (such as OC9–10–11-12-13) and those near the "Crateri Barbagallo" (OC15–16-17) outside the deposition zone. The Northern sites poorly preserved tephra erupted from the eruptions between 4/03 to 12/03, with plumes directed toward East and North-East. We can link the only significant layer found (OC23) to sedimentation from the 4/03 (E9) eruption plume, which dispersed to North-East, but may also have collected a small amount of pyroclasts from later eruptions (i.e., 7/03 and 10/03, E10 and E11 respectively).

Another two eruptive events that have been poorly recorded in the investigated area are the 14–15/03 and 17/03 eruptions (E13 and E14 respectively), whose plumes went to the East: only the areas closer to the SEC have recorded the deposition of fine ash solely from the edges of the plume (site OC 18) immersed in the snow which fell on 10/03 and the days following these two eruptions.

The second half of March was marked by poor weather conditions leading to the deposition of at least 1.5 m of snow in the summit area; the blanket of the 23–24/03 (E16) tephra fall-out is clearly recognizable from satellite images and easily correlated with the upper scoria bank, which also comprises the 31/03–1/04 (E17) eruption that marks the end of the studied period.

The opening phase of this eruptive crisis was recorded by a thin layer of red fine ash (at least 1 cm in the most proximal trenches) that we linked to the deposition from the 16/02 pyroclastic flow. This bed is easily recognizable in most of our outcrops and consequently was considered as a marker layer for tephra correlation.

Of all the 17 events between February and March 2021, tephra from only 5 eruptions was primarily preserved in the investigated area. Above the red fine grained ash layer, 4 main events were recognized: the eruptions E1, E8 and E16–17. However, although the eruption of 17/03 (E14) had a dispersion axis toward the investigated area, it appears as a thin level of fine lapilli within a thick layer of snow. Because of this feature and given its ephemeral and discontinuous nature, this tephra was not further studied. We correlate the first scoria bank with the eruptions E1 and E8 and the upper bank, deposited above approx. 1.5 m of snow in the most proximal deposits (which are also those located at highest altitudes), to the E16 and E17 eruptions (Fig. 4). The thickness of these layers varies between 15 cm and 10 cm. Even in this case at the base of this scoria level we found a very thin layer of red fine ash. As for the previous ones, we have linked it with the deposition of the elutriated materials by the pyroclastic flow of the 23–24/03 eruption.

5.2. Sedimentary features of proximal deposits

In general, scoria layers are massive, reverse-graded and clast-supported, without evidence of structures associated with lateral transport. The average size of clasts varies from coarse ash to lapilli (from bottom to top of each layer) including sporadic bomb-sized clasts that left no impact structures. Reverse grading likely recorded a gradual increase of the explosive activity (a resumption phase characterized by strombolian activity) and peak of intensity (paroxysmal phase associated with the formation of an ash plume) of the eruption as shown by the typical pattern of volcanic tremor of lava fountains (Alparone et al., 2003). On the contrary, the waning phase of the eruption was not recorded in proximal deposits studied here because of the rapid decrease in the eruption's intensity, also typical of Etna's paroxysmal activity. Deposits mainly consist of vesiculated juvenile material. The percentage of sideromelane is significantly lower when compared to data from other similar fountains (up to 30%; Polacci et al., 2019). We suggest that in proximal areas sedimentation of the tachylite prevails because of its higher density and higher terminal settling velocity with respect to sideromelane (Edwards et al., 2018; Edwards and Pioli, 2019). Measurements of the grain-size distribution in all our samples showed a great variability, a common feature of deposits in proximal areas. Samples were poorly sorted, and the distributions are bimodal. The coarse population has a wide range of Mdϕ spanning from −3.3 to −1.1, while the fine population had a narrower Mdϕ range around 1 and was likely due to contamination from ash remobilization or off-axis deposition from other plumes.

5.3. Significance of proximal sedimentation

Comparison of the February–April eruption data with previous eruptions show that they are representative of proximal sedimentation from high intensity paroxysmal events at Etna, allowing for a better quantification of the correlation between Mdϕ of tephra sedimenting from the plume with distance, along the dispersal axis. The general trend shows a dramatic decrease in grainsize (Fig. 9c) within the first 3 km. Unfortunately, previously published research on lava fountains rarely comprises proximal outcrops so it is not possible to directly compare our dataset with previous data. However, when added to a general Mdϕ vs. distance plot, the dataset matches well with medial data, allowing for the definition of a general trend, and some simulation of TGSD calculations, suggesting some key characteristics of sedimentation from plumes generated from lava fountains.

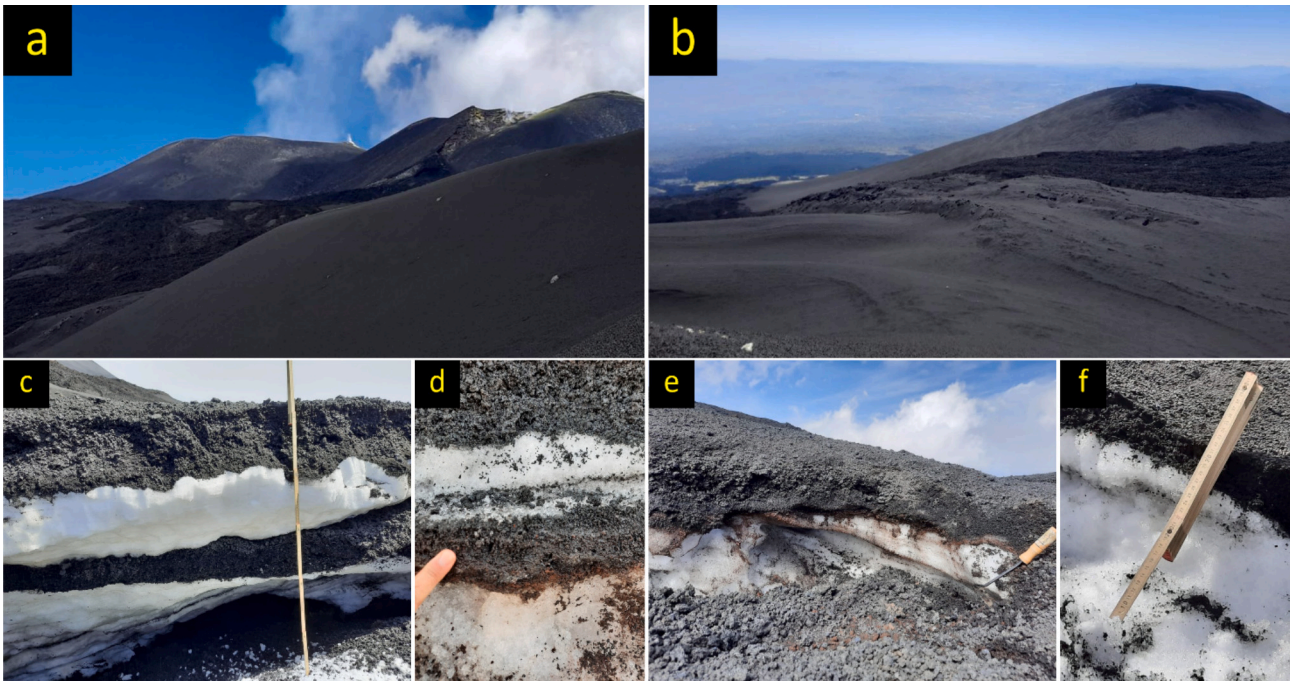

Fig. 3. Photos of the deposits. (a) and (b) showing the tephra blanket related to the last paroxysm of the eruptive crisis mantling the Etna summit area; (c), (d), (e) and (f) showing the tephra layers found on the trenches we dug (from near vent site OC1 in c to the last OC13 in f). (d) detail of site OC5 showing the thin layer of red fine ash at the base of the sequence; (e) shows the site OC9 in which we can see the second layer of red fine ash that can be found only in the latest sites. (For interpretation of the references to colour in this figure legend, the reader is referred to the web version of this article.)

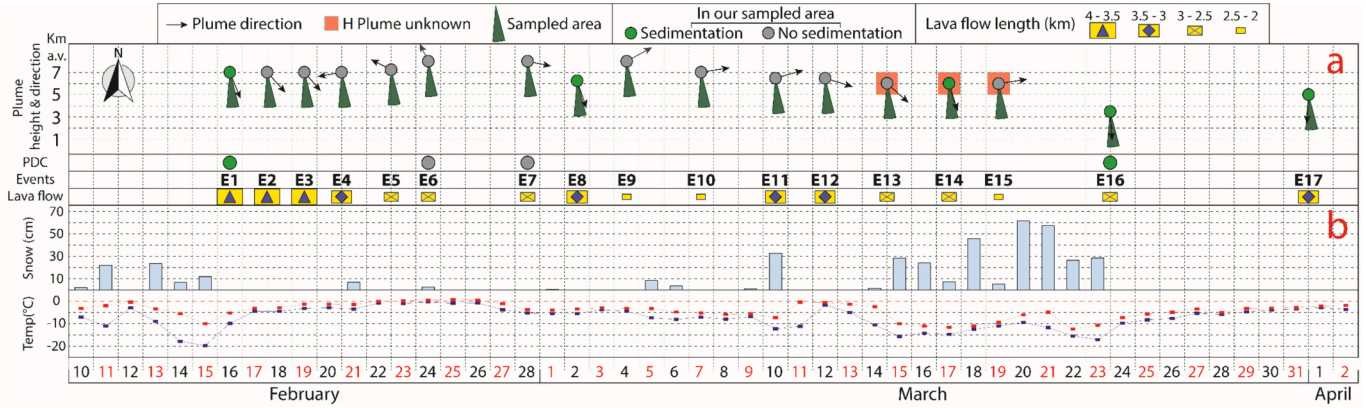

Fig. 4. (a) Summary of data available regarding Etna's February–April 2021 eruptive crisis (information from INGV-OE www.ct.ingv.it). Only 5 out of 17 eruptions have affected the investigated area (referred in the graph as "sedimentation"); (b) Monthly historical summary of weather conditions on Etna (information available on https://www.3bmeteo.com/meteo/etna/storico/202102) that provided useful information (temperatures constantly below 0 °C suggest no or limited snowmelt).

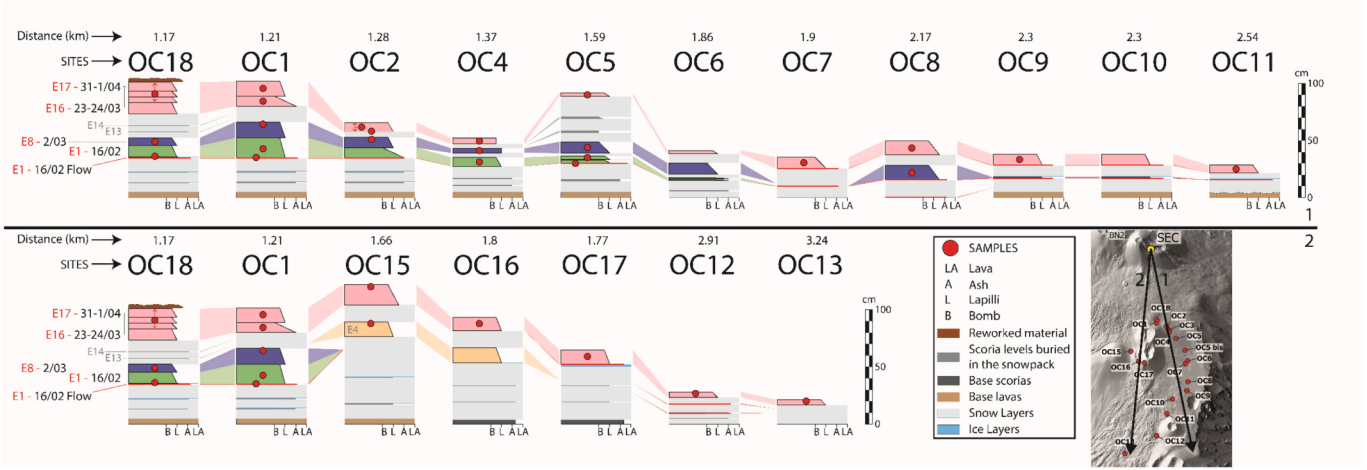

Fig. 5. Stratigraphic correlation of the February–April 2021 eruptive crisis reconstructed after the fieldwork. Section 1 moves along the "Pian del Lago" valley while section 2 passes near the "Crateri Barbagallo" (to include sites on the easternmost and the westernmost portion of the analyzed area respectively).

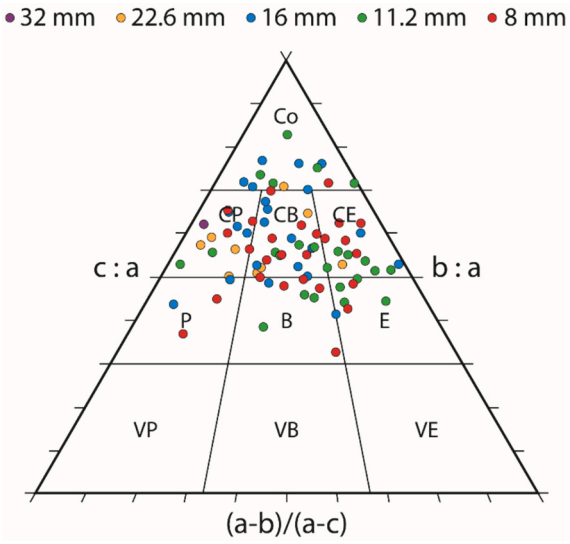

Fig. 6. Morphology of analyzed clasts (Sneed and Folk, 1958). Colors in the graph refer to the analyzed grain size classes (32 mm violet dots, 22.6 mm yellow dots, 16 mm blue dots, 11.2 mm green dots, 8 mm red dots). Morphology classes: *Co*) compact; V) very; P) platy; B) bladed; E) elongated. Letters a, b and c represent the long, intermediate and short orthogonal axes of each particle respectively. (For interpretation of the references to colour in this figure legend, the reader is referred to the web version of this article.)

Fitting data from Medial-distal distances provide significantly different curves than more complete sequences and underestimate the contribution of proximal sedimentation.

The dramatic increase in grainsize with distance of tephra at proximal locations define a high slope part of the curve which suggests significant effects on the assessment of TGSDs, with a potential underestimation of the median grainsize of erupted material up to 2 ϕ.

We envisage the necessity for further dedicated studies on proximal sedimentation to fully estimate and eventually develop more accurate TGSDs models. Finally, we note that the componentry of proximal samples is enriched in tachylite (i.e. dense) juvenile scoria, suggesting that the estimation of the relative proportion of the juvenile components erupted in a single event should be based on the analysis of samples distributed at different distances from the vent.

6. Conclusions

Based on our field observations and laboratory analyses we can conclude that:

The tephra layers found at the investigated sites are related to the tephra deposition from the February–April 2021 eruptive crisis. These layers are related to eruptions that dispersed pyroclasts along a southerly direction (E1, E8, E14, E16 and E17). We were able to reconstruct the sequence of these eruptions based on remote sensing data and the presence of snow and ice blankets.

All the deposits resulted in a reverse grading. They record: I) the initial stages of the eruptions marked by a dominant strombolian activity which favors the deposition of fine materials and sporadic bomb-sized clasts; II) the increase and peak of the intensity with the transition from strombolian activity to lava fountains, that leads to the sedimentation of coarse pyroclasts. The final stages are not recorded in the deposits because of the abrupt decrease in the eruption intensity.

These proximal deposits showed a prevalence of juvenile material mainly composed of tachylite clasts with respect to the sideromelane. This feature contrasts with what has been observed in medial and distal deposits that always show a predominance of sideromelane. We linked this variation to the difference in densities between these two components. However, further studies are needed to fully understand the fragmentation mechanisms of the mafic eruption and how it affects these two magma components.

GSDs derived from our deposits are multimodal. This is a common feature of deposits that are close to the eruptive source, which collect material resulting from both different direct sedimentation processes (ballistic blocks, clasts from column edges and plume fall-out material) and reworking processes (mainly wind reworking in our case).

After deconvolution of the GSDs, the Mdϕ parameters related to the main population (related to the plume fall-out sedimentation) are likely representative of the proximal trend of Etna's high-intensity paroxysms in the last decade.

Our data demonstrate that the analysis of proximal tephra fall deposit is fundamental for a proper assessment of the Total GSD. The lack of samples from proximal zones can cause a shifting toward fine sizes in the whole grain-size tephra deposit of around 2 ϕ units. An appropriate evaluation of the TGSD could reduce the uncertainty related to the quantification of ESPs and therefore enhance the volcanic ash dispersion

Table 2
List of empirical grainsize parameters. **MdΦ** represent the median diameter in phi and **σϕ** is the standard deviation of the distribution; **F1** and **F2** are values representing the weight percentage cumulative sum of particles finer than 1 mm (0ϕ) and 63 μm (4ϕ), respectively (Walker, 1983).

Outcrop Levels	Decimal degrees coordinates		MdΦ	σΦ	F1	F2
	Latitude	Longitude				
OC1-1a	37.7366	15.001833	−2.80	2.19	11.93	0.48
OC1-1b	37.7366	15.001833	−3.56	1.12	2.16	0.08
OC1–2a	37.7366	15.001833	−3.36	2.37	10.41	0.19
OC1–2b	37.7366	15.001833	−2.69	1.02	25.47	2.00
OC1-S_Base	37.7366	15.001833	−2.32	1.34	2.90	0.07
OC2-1Top	37.736167	15.003633	−3.54	1.34	1.89	0.02
OC2-2a	37.736167	15.003633	−1.21	1.61	7.33	0.10
OC2-2tot	37.736167	15.003633	−2.31	1.36	4.06	0.06
OC4-1a	37.735417	15.0041	−1.65	1.82	6.65	0.11
OC4-1b	37.735417	15.0041	−1.68	1.96	5.60	0.00
OC4-2tot	37.735417	15.0041	−1.07	1.74	8.50	0.14
OC5-Before_S	37.7345	15.005267	−2.30	1.58	4.75	0.00
OC5-S_Base	37.7345	15.005267	−0.65	1.75	13.31	0.00
OC5-1a	37.7345	15.005267	−2.81	2.03	3.33	0.00
OC5-1b	37.7345	15.005267	−3.00	1.51	3.30	0.05
OC5-2tot	37.7345	15.005267	−2.62	1.85	5.32	0.00
OC 7-2tot	37.731067	15.006883	−2.65	1.60	9.44	0.23
OC 8-1b	37.728617	15.0073	−0.54	1.91	8.11	0.14
OC 8-2tot	37.728617	15.0073	−2.09	1.72	16.01	1.24
OC 9-2tot	37.727433	15.007133	−2.45	1.64	13.56	0.93
OC 11–2tot	37.72425	15.00365	−2.71	1.42	8.02	0.29
OC 12-2tot	37.721283	15.001933	−2.03	1.78	15.81	0.57
OC 13-2tot	37.718833	14.996383	−1.68	1.37	13.69	0.35
OC 15-NO_S	37.7328	14.997433	−1.83	1.25	9.82	0.10
OC 15–2 top	37.7328	14.997433	−1.85	1.18	8.02	0.14
OC 16-2tot	37.731383	14.998783	−4.09	2.38	6.93	0.04
OC 17-2tot	37.7312	14.999783	−2.80	0.80	2.84	0.04
OC 18-S_Base	37.73705	15.002	−2.39	1.58	11.44	0.10
OC 18-1b	37.73705	15.002	−3.50	0.84	2.93	0.02
OC 18–2 tot	37.73705	15.002	−2.68	1.33	7.22	0.06

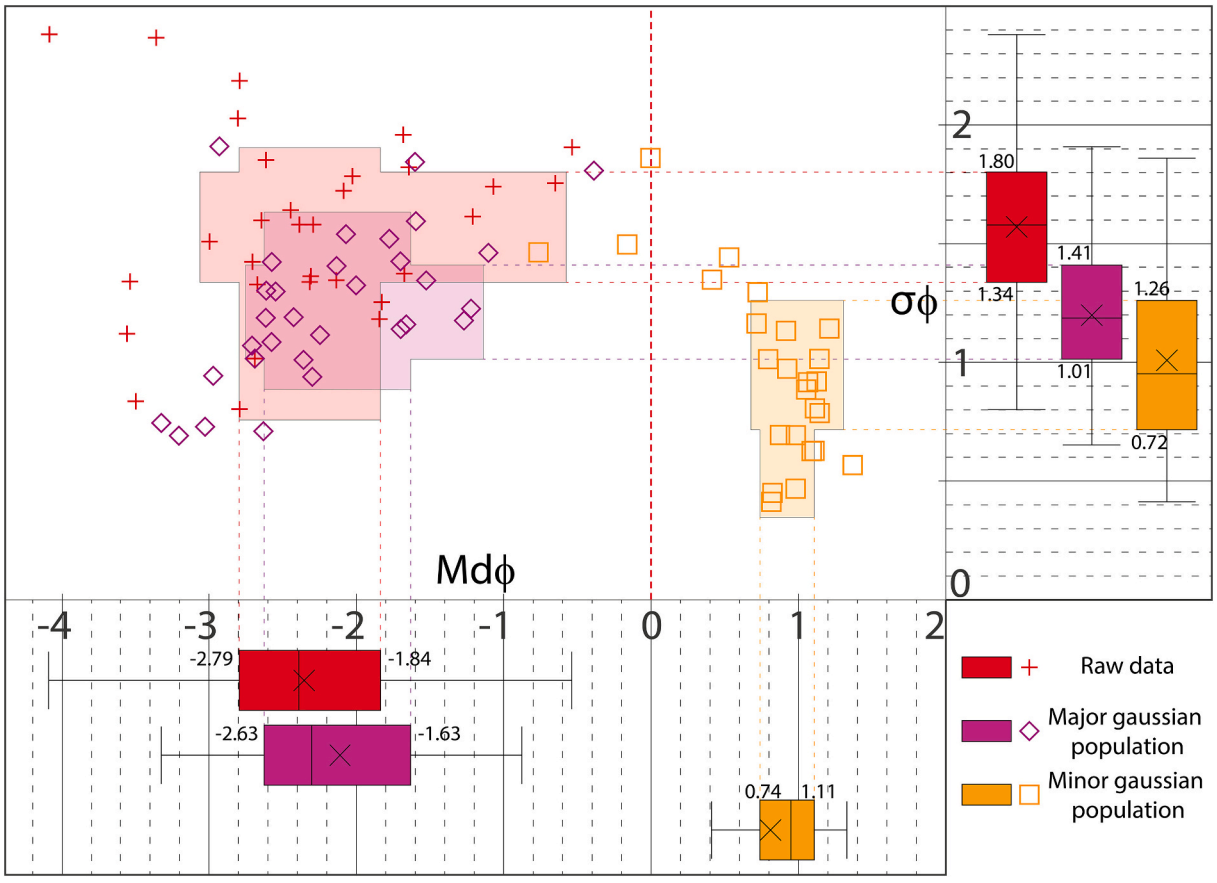

Fig. 7. Comparison between raw data and deconvoluted statistical parameters (**Mdϕ** and **σϕ**). Raw data result more scattered than the data obtained after deconvolution (Purple diamonds). In part there is an overlap between the raw and deconvolution-derived parameters of the major gaussian population of the particle size distribution. The minor gaussian population identifies a separate trend. Numbers in the boxplots refer to the range in which 50% of the data can be found (25th and 75th percentiles). (For interpretation of the references to colour in this figure legend, the reader is referred to the web version of this article.)

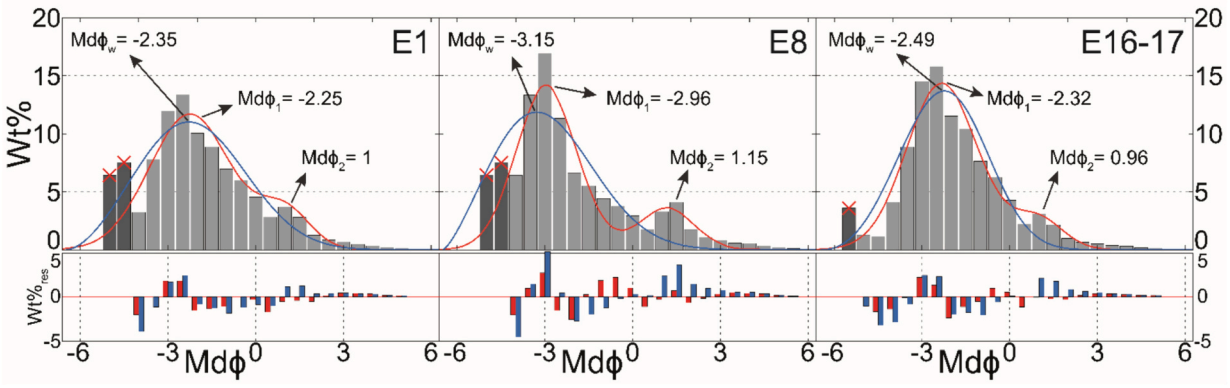

Fig. 8. Averaged Proximal Grain-Size Distributions (PGSD) for the E1, E8 and E16–17 eruptions of Etna during February–April 2021 and their bi-Gaussian deconvolution (red line) and Weibull distribution (blue line). Graph below shows the residual (in wt%) between the two deconvolution curves and the real distribution. Distributions are obtained by calculating the weighted average GSD of the layers related to these eruptions at each site. Largest grain-size classes (dark gray) were not considered for the deconvolution. (For interpretation of the references to colour in this figure legend, the reader is referred to the web version of this article.)

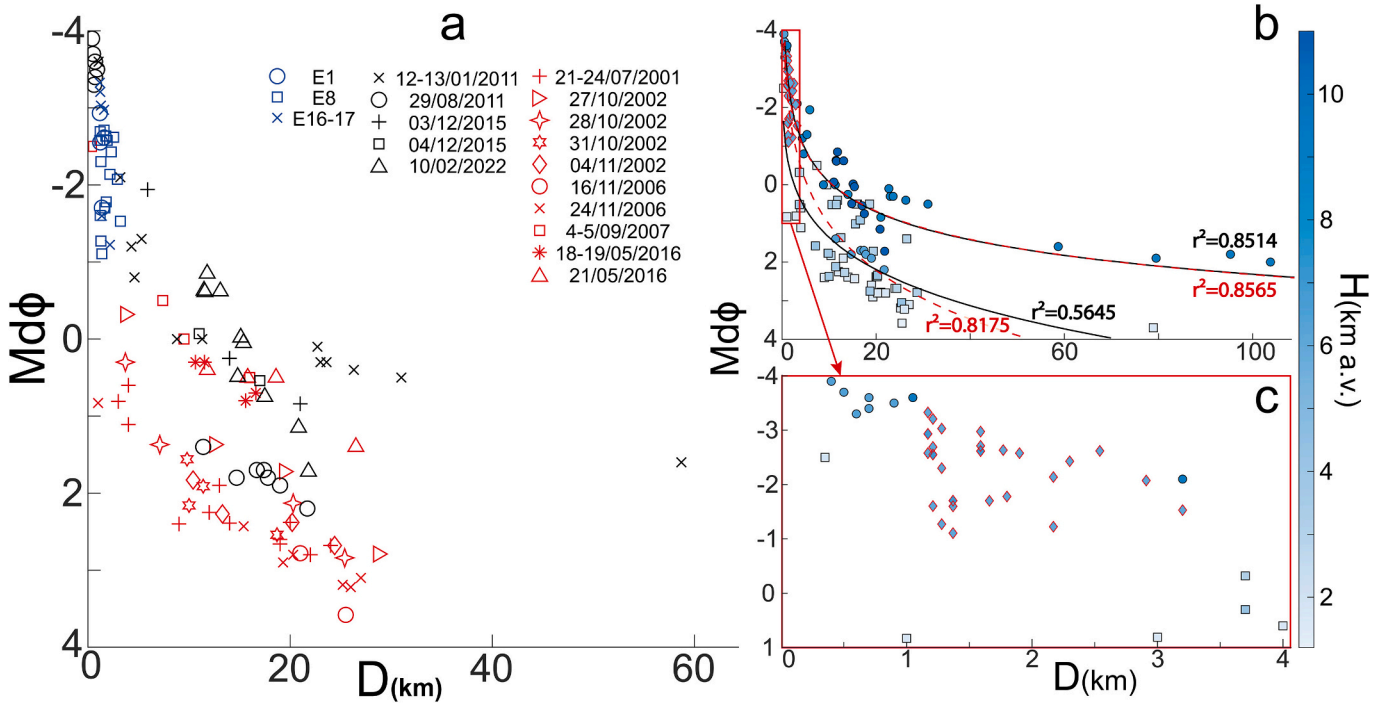

Fig. 9. Mdϕ variation as a function of the distance (D) from the active vent. (a) summary of Etna's tephra-fallout deposits considered. Symbols in red and black refer to past eruptions of which the column was lower and equal or higher than 5 km respectively, while blue symbols refer to our proximal samples. (b) fitting with exponential curves computed with (red dashed curves and R^2) and without (black curves and R^2) the contribution of our proximal samples (red contoured diamonds), for both eruptions with column height greater (circles) and lesser (squares) than 5 km a.v. (column height above the vent is also highlighted by the blue tone scale); (c) zoom of (b) on our proximal samples that align with the trend outlined by samples from high intensity paroxysm. (For interpretation of the references to colour in this figure legend, the reader is referred to the web version of this article.)

Table 3
Fitting parameters of the power law curves in Fig. 9b and the related R^2.

Power law Equation $f(x) = a^*x^b + c$	Fitting parameters			R^2
	a	b	c	
Literature data (H < 5)	4.3891	0.1724	−5.1626	0.5645
Literature data (H < 5) and Proximal data	17.1127	0.0812	−19.6017	0.8175
Literature data (H > 5)	−15.8324	−0.0886	12.8447	0.8514
Literature data (H > 5) and Proximal data	−18.8025	−0.0706	15.9069	0.8565

and sedimentation predictive models.

CRediT authorship contribution statement

Francesco Amadio: Writing – original draft, Visualization, Validation, Investigation, Formal analysis, Data curation, Conceptualization. **Laura Pioli:** Writing – review & editing, Supervision, Project administration, Funding acquisition, Formal analysis, Data curation, Conceptualization. **Simona Scollo:** Writing – review & editing, Supervision, Project administration, Funding acquisition, Formal analysis, Data curation, Conceptualization.

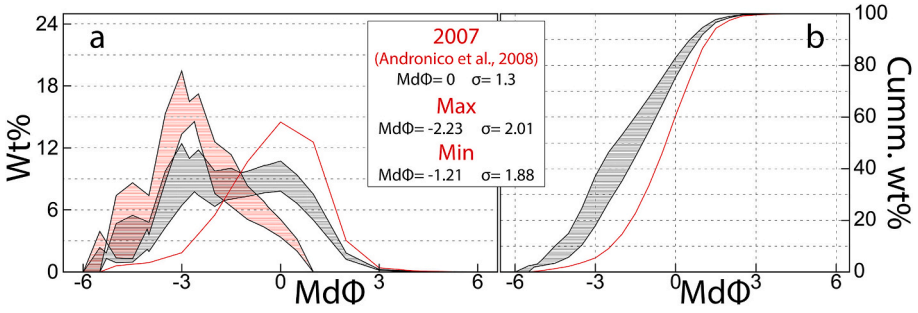

Fig. 10. a) probability density function and b) cumulative density function. Comparison between the **total grain-size distribution** of the 4–5 September 2007 eruption from the published data of Andronico et al., 2008 (red solid line) and our Proximal Grain-Size Distribution (red area in a comprising the PGSD of E1, E8 and E16–17 layers). Black area in Fig. 10 a and b represents the Total grain-size distribution resulting from the merging of these two datasets with increasing percentage of contribution of Proximal GSD, from 40% to 60% of particles mass. (For interpretation of the references to colour in this figure legend, the reader is referred to the web version of this article.)

Declaration of competing interest

The authors declare that they have no known competing financial interests or personal relationships that could have appeared to influence the work reported in this paper.

Data availability

Data will be made available on request.

Acknowledgments

This publication was produced during F.A. PhD course, XXXVIII cycle, in “Scienze e Tecnologie della Terra e dell’Ambiente” at the University of Cagliari, with the support of a scholarship funded by Ministerial Decree No. 351 of 9.4.2022, under the PNRR - funded by the European Union – NextGenerationEU. The work was partially supported by the project F73C23001610007 funded by Fondazione di Sardegna (to L. Pioli). This research was also performed in the framework of the INGV Project “Pianeta Dinamico” (D53J19000170001), funded by MUR (“Ministero dell’Università e della Ricerca, Fondo finalizzato al rilancio degli investimenti delle amministrazioni centrali dello Stato e allo sviluppo del Paese, legge 145/2018”).

We acknowledge Gabriele Schirra for performing density and shape measurement and componentry as part of his undergraduate thesis at UNICA. We thank the technicians and technologists in charge of the INGV-OE camera network. We are also grateful to the volcanologists of INGV-OE who regularly collect data during volcanic events and often work long hours. We would also like to thank the administrative and technical support of INGV-OE that enables us to collect and analyze data. The authors also thank Stephen Conway, an English native speaker reviewing the paper for INGV-OE.

Appendix A. Supplementary data

Supplementary data to this article can be found online at https://doi.org/10.1016/j.jvolgeores.2024.108164.

References

Aiuppa, A., Lo Bue Trisciuzzi, G., Alparone, S., Bitetto, M., Coltelli, M., Delle Donne, D., Pecora, E., 2023. A SO2 flux study of the Etna volcano 2020–2021 paroxysmal sequences. Front. Earth Sci. 11, 1115111 https://doi.org/10.3389/feart.2023.1115111.

Alparone, S., Andronico, D., Lodato, L., Sgroi, T., 2003. Relationship between tremor and volcanic activity during the Southeast Crater eruption on Mount Etna in early 2000. J. Geophys. Res. Solid Earth 108 (B5). https://doi.org/10.1029/2002JB001866.

Andronico, D., Del Carlo, P., Coltelli, M., 1999, January. The 22 July 1998 fire fountain episode at Voragine Crater (Mt. Etna, Italy). In: VMSG-Annual Meeting (pp. 5-6)..

Andronico, D., Cristaldi, A., Scollo, S., 2008. The 4–5 September 2007 lava fountain at south-east crater of Mt Etna, Italy. J. Volcanol. Geotherm. Res. 173 (3–4), 325–328. https://doi.org/10.1016/j.jvolgeores.2008.02.004.

Andronico, D., Scollo, S., Cristaldi, A., Ferrari, F., 2009. Monitoring ash emission episodes at Mt. Etna: the 16 November 2006 case study. J. Volcanol. Geotherm. Res. 180 (2–4), 123–134. https://doi.org/10.1016/j.jvolgeores.2008.10.019.

Andronico, D., Scollo, S., Cristaldi, A., Lo Castro, M.D., 2014a. Representivity of incompletely sampled fall deposits in estimating eruption source parameters: a test using the 12–13 January 2011 lava fountain deposit from Mt. Etna volcano, Italy. Bull. Volcanol. 76, 1–14. https://doi.org/10.1007/s00445-014-0861-3.

Andronico, D., Scollo, S., Castro, M.D.L., Cristaldi, A., Lodato, L., Taddeucci, J., 2014b. Eruption dynamics and tephra dispersal from the 24 November 2006 paroxysm at South-East Crater, Mt Etna, Italy. J. Volcanol. Geotherm. Res. 274, 78–91. https://doi.org/10.1016/j.jvolgeores.2014.01.009.

Andronico, D., Cannata, A., Di Grazia, G., Ferrari, F., 2021. The 1986–2021 paroxysmal episodes at the summit craters of Mt. Etna: Insights into volcano dynamics and hazard. Earth-Sci. Rev. 220, 103686 https://doi.org/10.1016/j.earscirev.2021.103686.

Barsotti, S., Neri, A., Scire, J.S., 2008. The VOL-CALPUFF model for atmospheric ash dispersal: 1. Approach and physical formulation. J. Geophys. Res. Solid Earth 113 (B3). https://doi.org/10.1029/2006JB004623.

Behncke, B., Branca, S., Corsaro, R.A., De Beni, E., Miraglia, L., Proietti, C., 2014. The 2011–2012 summit activity of Mount Etna: Birth, growth and products of the new SE crater. J. Volcanol. Geotherm. Res. 270, 10–21. https://doi.org/10.1016/j.jvolgeores.2013.11.012.

Blong, R.J., 1984. Volcanic Hazards: A Sourcebook on the Effects of Eruptions. Elsevier. ISBN 0-12-107-180-4.

Bonaccorso, A., Aloisi, M., 2021. Tracking magma storage: new perspectives from 40 years (1980–2020) of ground deformation source modeling on Etna volcano. Front. Earth Sci. 9, 638742 https://doi.org/10.3389/feart.2021.638742.

Bonaccorso, A., Carleo, L., Currenti, G., Sicali, A., 2021. Magma migration at shallower levels and lava fountains sequence as revealed by borehole dilatometers on Etna volcano. Front. Earth Sci. 9, 740505 https://doi.org/10.3389/feart.2021.740505.

Bonadonna, C., Phillips, J.C., 2003. Sedimentation from strong volcanic plumes. J. Geophys. Res. Solid Earth 108 (B7). https://doi.org/10.1029/2002JB002034.

Bonadonna, C., Ernst, G.G.J., Sparks, R.S.J., 1998. Thickness variations and volume estimates of tephra fall deposits: the importance of particle Reynolds number. J. Volcanol. Geotherm. Res. 81 (3–4), 173–187. https://doi.org/10.1016/S0377-0273(98)00007-9.

Bonadonna, C., Connor, C.B., Houghton, B.F., Connor, L., Byrne, M., Laing, A., Hincks, T. K., 2005. Probabilistic modeling of tephra dispersal: Hazard assessment of a multiphase rhyolitic eruption at Tarawera, New Zealand. J. Geophys. Res. Solid Earth 110 (B3). https://doi.org/10.1029/2003JB002896.

Bonadonna, C., Biass, S., Costa, A., 2015a. Physical characterization of explosive volcanic eruptions based on tephra deposits: propagation of uncertainties and sensitivity analysis. J. Volcanol. Geotherm. Res. 296, 80–100. https://doi.org/10.1016/j.jvolgeores.2015.03.009.

Bonadonna, C., Costa, A., 2013. Modeling Tephra Sedimentation from Volcanic Plumes. Modeling Volcanic Processes: The Physics and Mathematics of Volcanism. [s.l.]. Cambridge Univ. Press, pp. 173–202. ISBN 978-0-521-89543-9.

Bonadonna, C., Costa, A., Folch, A., Koyaguchi, T., 2015b. Tephra dispersal and sedimentation. In: Sigurdsson, H., Houghton, B., McNutt, S.R., Rymer, H., Stix, J. (Eds.), The Encyclopedia of Volcanoes. Academic Press, pp. 587–597. https://doi.org/10.1016/B978-0-12-385938-9.00033-X.

Branca, S., Del Carlo, P., 2005. Types of eruptions of Etna volcano AD 1670–2003: implications for short-term eruptive behaviour. Bull. Volcanol. 67, 732–742. https://doi.org/10.1007/s00445-005-0412-z.

Branca, S., De Beni, E., Proietti, C., 2013. The large and destructive 1669 AD eruption at Etna volcano: reconstruction of the lava flow field evolution and effusion rate trend. Bull. Volcanol. 75, 1–16. https://doi.org/10.1007/s00445-013-0694-5.

Branca, S., De Beni, E., Chester, D., Duncan, A., Lotteri, A., 2017. The 1928 eruption of Mount Etna (Italy): Reconstructing lava flow evolution and the destruction and recovery of the town of Mascali. J. Volcanol. Geotherm. Res. 335, 54–70. https://doi.org/10.1016/j.jvolgeores.2017.02.002.

Bursik, M.I., Sparks, R.S.J., Gilbert, J.S., Carey, S.N., 1992. Sedimentation of tephra by volcanic plumes: I. Theory and its comparison with a study of the Fogo a plinian deposit, Sao Miguel (Azores). Bull. Volcanol. 54, 329–344. https://doi.org/10.1007/BF00301486.

Calvari, S., Nunnari, G., 2022. Comparison between automated and manual detection of lava fountains from fixed monitoring thermal cameras at Etna Volcano, Italy. Remote Sens. 14 (10), 2392 https://doi.org/10.3390/rs14102392.

Calvari, S., Bonaccorso, A., Ganci, G., 2021. Anatomy of a paroxysmal lava fountain at Etna volcano: the case of the 12 March 2021, episode. Remote Sens. 13 (15), 3052. https://doi.org/10.3390/rs13153052.

Casadevall, T.J., 1994. The 1989–1990 eruption of Redoubt Volcano, Alaska: impacts on aircraft operations. J. Volcanol. Geotherm. Res. 62 (1–4), 301–316. https://doi.org/10.1016/0377-0273(94)90038-8.

Coltelli, M., Del Carlo, P., Vezzoli, L., 1998. Discovery of a Plinian basaltic eruption of Roman age at Etna volcano, Italy. Geol 26 (12), 1095–1098. https://doi.org/10.1130/0091-7613(1998)026<1095:DOAPBE>2.3.CO;2.

Coltelli, M., Del Carlo, P., Vezzoli, L., 2000. Stratigraphic constraints for explosive activity in the past 100 ka at Etna Volcano, Italy. Int. J. Earth Sci. 89, 665–677. https://doi.org/10.1007/s005310000117.

Coltelli, M., Del Carlo, P., Pompilio, M., Vezzoli, L.U., 2005. Explosive eruption of a picrite: the 3930 BP subplinian eruption of Etna volcano (Italy). Geophys. Res. Lett. 32 (23) https://doi.org/10.1029/2005GL024271.

Corsaro, R.A., Miraglia, L., 2022. Near real-time petrologic monitoring on volcanic glass to infer magmatic processes during the February–April 2021 paroxysms of the South-East Crater, Etna. Front. Earth Sci. 10, 828026 https://doi.org/10.3389/feart.2022.828026.

Corradini, S., Guerrieri, L., Lombardo, V., Merucci, L., Musacchio, M., Prestifilippo, M., Stelitano, D., 2018. Proximal monitoring of the 2011–2015 Etna lava fountains using MSG-SEVIRI data. Geosciences 8 (4), 140. https://doi.org/10.3390/geosciences8040140.

Costa, A., Macedonio, G., Folch, A., 2006. A three-dimensional Eulerian model for transport and deposition of volcanic ashes. EPSL 241 (3–4), 634–647. https://doi.org/10.1016/j.epsl.2005.11.019.

Del Bello, E., Taddeucci, J., Merrison, J.P., Alois, S., Iversen, J.J., Scarlato, P., 2018. Experimental simulations of volcanic ash resuspension by wind under the effects of atmospheric humidity. Sci. Rep. 8 (1), 14509. https://doi.org/10.1038/s41598-018-32807-2.

Dominguez, L., Bonadonna, C., Forte, P., Jarvis, P.A., Cioni, R., Mingari, L., Panebianco, J.E., 2020. Aeolian remobilisation of the 2011-Cordón Caulle tephra-fallout deposit: example of an important process in the life cycle of volcanic ash. Front. Earth Sci. 7, 343. https://doi.org/10.3389/feart.2019.00343.

Edwards, M.J., Pioli, L., 2019. Magma and tephra characteristics for the 17–25 May 2016 Mt Etna eruption. Data Brief 22, 65–71. https://doi.org/10.1016/j.dib.2018.11.093.

Edwards, M.J., Pioli, L., Andronico, D., Scollo, S., Ferrari, F., Cristaldi, A., 2018. Shallow factors controlling the explosivity of basaltic magmas: the 17–25 May 2016 eruption of Etna Volcano (Italy). J. Volcanol. Geotherm. Res. 357, 425–436. https://doi.org/10.1016/j.jvolgeores.2018.05.015.

Folch, A., 2012. A review of tephra transport and dispersal models: Evolution, current status, and future perspectives. J. Volcanol. Geotherm. Res. 235, 96–115. https://doi.org/10.1016/j.jvolgeores.2012.05.020.

Folch, A., Mingari, L., Osores, M.S., Collini, E., 2014. Modeling volcanic ash resuspension–application to the 14–18 October 2011 outbreak episode in Central Patagonia, Argentina. Nat. Hazard Earth Sys. 14 (1), 119–133. https://doi.org/10.5194/nhess-14-119-2014.

Guerrieri, L., Corradini, S., Theys, N., Stelitano, D., Merucci, L., 2023. Volcanic clouds characterization of the 2020–2022 sequence of Mt. Etna lava fountains using MSG-SEVIRI and products' cross-comparison. Remote Sens. 15 (8), 2055 https://doi.org/10.3390/rs15082055.

Guffanti, M., Mayberry, G.C., Casadevall, T.J., Wunderman, R., 2009. Volcanic hazards to airports. Nat. Hazards 51, 287–302. https://doi.org/10.1007/s11069-008-9254-2.

Houghton, B.F., Wilson, C.J.N., 1989. A vesicularity index for pyroclastic deposits. Bull. Volcanol. 51, 451–462. https://doi.org/10.1007/BF01078811. https://cin.floq.live/event/iugg2023berlin/daily_program_iavcei?objectClass=timeslot&objectId=649483f764c73802ac74889c&type=detail.

Inman, D.L., 1952. Measures for describing the size distribution of sediments. J. Sed. https://doi.org/10.1306/D42694DB-2B26-11D7-8648000102C1865D.

Jarvis, P.A., Bonadonna, C., Dominguez, L., Forte, P., Frischknecht, C., Bran, D., Wallace, K.L., 2020. Aeolian remobilisation of volcanic ash: outcomes of a workshop in the Argentinian Patagonia. Front. Earth Sci. 569 https://doi.org/10.3389/feart.2020.575184.

Liu, E.J., Cashman, K.V., Beckett, F.M., Witham, C.S., Leadbetter, S.J., Hort, M.C., Guðmundsson, S., 2014. Ash mists and brown snow: Remobilization of volcanic ash from recent Icelandic eruptions. J. Geophys. Res. Atmos. 119 (15), 9463–9480. https://doi.org/10.1002/2014JD021598.

Marchese, F., Genzano, N., Neri, M., Falconieri, A., Mazzeo, G., Pergola, N., 2019. A multi-channel algorithm for mapping volcanic thermal anomalies by means of Sentinel-2 MSI and Landsat-8 OLI data. Remote Sens. 11 (23), 2876. https://doi.org/10.3390/rs11232876.

Marchese, F., Filizzola, C., Lacava, T., Falconieri, A., Faruolo, M., Genzano, N., Neri, M., 2021. Correction: Marchese et al. Mt. Etna Paroxysms of February–April 2021 Monitored and Quantified through a Multi-Platform Satellite Observing System. Remote Sens. 13, 3074. *14*(12), 2746. https://doi.org/10.3390/rs13163074.

Massimetti, F., Coppola, D., Laiolo, M., Valade, S., Cigolini, C., Ripepe, M., 2020. Volcanic hot-spot detection using SENTINEL-2: a comparison with MODIS–MIROVA thermal data series. Remote Sens. 12 (5), 820 https://doi.org/10.3390/rs12050820.

Mastin, L.G., Guffanti, M., Servranckx, R., Webley, P., Barsotti, S., Dean, K., Waythomas, C.F., 2009. A multidisciplinary effort to assign realistic source parameters to models of volcanic ash-cloud transport and dispersion during eruptions. J. Volcanol. Geotherm. Res. 186 (1–2), 10–21. https://doi.org/10.1016/j.jvolgeores.2009.01.008.

Panebianco, J.E., Mendez, M.J., Buschiazzo, D.E., Bran, D., Gaitán, J.J., 2017. Dynamics of volcanic ash remobilisation by wind through the Patagonian steppe after the eruption of Cordón Caulle, 2011. Sci. Rep. 7 (1), 45529 https://doi.org/10.1038/srep45529.

Parfitt, E.A., 1998. A study of clast size distribution, ash deposition and fragmentation in a Hawaiian-style volcanic eruption. J. Volcanol. Geotherm. Res. 84 (3–4), 197–208. https://doi.org/10.1016/S0377-0273(98)00042-0.

Pioli, L., Harris, A.J., 2019. Real-time geophysical monitoring of particle size distribution during volcanic explosions at Stromboli volcano (Italy). Front. Earth Sci. 7, 52. https://doi.org/10.3389/feart.2019.00052.

Pioli, L., Bonadonna, C., Pistolesi, M., 2019. Reliability of total grain-size distribution of tephra deposits. Sci. Rep. 9 (1), 10006 https://doi.org/10.1038/s41598-019-46125-8.

Polacci, M., Pioli, L., Rosi, M., 2003. The Plinian phase of the Campanian Ignimbrite eruption (Phlegrean Fields, Italy): evidence from density measurements and textural characterization of pumice. Bull. Volcanol. 65, 418–432. https://doi.org/10.1007/s00445-002-0268-4.

Polacci, M., Corsaro, R.A., Andronico, D., 2006. Coupled textural and compositional characterization of basaltic scoria: Insights into the transition from Strombolian to fire fountain activity at Mount Etna, Italy. Geology 34 (3), 201–204. https://doi.org/10.1130/G22318.1.

Polacci, M., Andronico, D., de Michieli Vitturi, M., Taddeucci, J., Cristaldi, A., 2019. Mechanisms of Ash Generation at Basaltic Volcanoes: the Case of Mount Etna, Italy. Front. Earth Sci. 7, 193. https://doi.org/10.3389/feart.2019.00193.

Scollo, S., Del Carlo, P., Coltelli, M., 2007. Tephra fallout of 2001 Etna flank eruption: Analysis of the deposit and plume dispersion. J. Volcanol. Geotherm. Res. 160 (1–2), 147–164. https://doi.org/10.1016/j.jvolgeores.2006.09.007.

Scollo, S., Folch, A., Costa, A., 2008a. A parametric and comparative study of different tephra fallout models. J. Volcanol. Geotherm. Res. 176 (2), 199–211. https://doi.org/10.1016/j.jvolgeores.2008.04.002.

Scollo, S., Tarantola, S., Bonadonna, C., Coltelli, M., Saltelli, A., 2008b. Sensitivity analysis and uncertainty estimation for tephra dispersal models. J. Geophys. Res. Solid Earth 113 (B6). https://doi.org/10.1029/2006JB004864.

Scollo, S., Coltelli, M., Bonadonna, C., Del Carlo, P., 2013. Tephra hazard assessment at Mt. Etna (Italy). Nat. Hazard Earth Sys. 13 (12), 3221–3233. https://doi.org/10.5194/nhess-13-3221-2013.

Scollo, S., Prestifilippo, M., Bonadonna, C., Cioni, R., Corradini, S., Degruyter, W., Pecora, E., 2019. Near-real-time tephra fallout assessment at Mt. Etna, Italy. Remote Sens. *11* (24), 2987. https://doi.org/10.3390/rs11242987.

Sheridan, M.F., Wohletz, K.H., Dehn, J., 1987. Discrimination of grain-size subpopulations in pyroclastic deposits. Geology 15 (4), 367–370. https://doi.org/10.1130/0091-7613(1987)15<367:DOGSIP>2.0.CO;2.

Sneed, E.D., Folk, R.L., 1958. Pebbles in the lower Colorado River, Texas a study in particle morphogenesis. J. Geol. 66 (2), 114–150. https://doi.org/10.1086/626490.

Sparks, R.S.J., Bursik, M.I., Ablay, G.J., Thomas, R.M.E., Carey, S.N., 1992. Sedimentation of tephra by volcanic plumes. Part 2: controls on thickness and grain-size variations of tephra fall deposits. Bull. Volcanol. 54, 685–695. https://doi.org/10.1007/BF00430779.

Sparks, R.S.J., Barclay, J., Jaupart, C.P.M.A., Mader, H.M., Phillips, J.C., Sturtevant, B., 1994. Physical aspects of magma degassing. Mineral. Soci. Am. Rev. Mineral. 30, 413–445. https://doi.org/10.1515/9781501509674-017.

Stein, A.F., Draxler, R.R., Rolph, G.D., Stunder, B.J., Cohen, M.D., Ngan, F., 2015. NOAA's HYSPLIT atmospheric transport and dispersion modeling system. B. Am. Meteorol. Soc. 96 (12), 2059–2077. https://doi.org/10.1175/BAMS-D-14-00110.1.

Taddeucci, J., Pompilio, M., Scarlato, P., 2002. Monitoring the explosive activity of the July–August 2001 eruption of Mt. Etna (Italy) by ash characterization. Geophys. Res. Lett. 29 (8), 71. https://doi.org/10.1029/2001GL014372.

Taddeucci, J., Edmonds, M., Houghton, B., James, M.R., Vergniolle, S., 2015. Hawaiian and Strombolian Eruptions (Chapter 27, pp. 485-503). In: Sigurdsson, H., Houghton, B., McNutt, S.R., Rymer, H., Stix, J. (Eds.), The Encyclopedia of Volcanoes, Second edition. Academic Press, Waltham, MA, USA. https://doi.org/10.1016/B978-0-12-385938-9.00001-8.

Viccaro, M., Calcagno, R., Garozzo, I., Giuffrida, M., Nicotra, E., 2015. Continuous magma recharge at Mt. Etna during the 2011–2013 period controls the style of volcanic activity and compositions of erupted lavas. Mineral. Petrol. 109, 67–83. https://doi.org/10.1007/s00710-014-0352-4.

Walker, G.P., 1983. Ignimbrite types and ignimbrite problems. J. Volcanol. Geotherm. Res. 17 (1–4), 65–88. https://doi.org/10.1016/0377-0273(83)90062-8.

Wohletz, K.H., Sheridan, M.F., Brown, W.K., 1989. Particle size distributions and the sequential fragmentation/transport theory applied to volcanic ash. J. Geophys. Res. 94 (B11), 15703–15721. https://doi.org/10.1029/JB094iB11p15703.